Preprints (www.preprints.org) | NOT PEER-REVIEWED | Posted: 5 December 2019 doi:10.20944/preprints201912.0059.v1

Article

Classification of Hyperspectral Image Based on Double-Branch Dual-Attention Mechanism Network

Rui Li [1,*], Shunyi Zheng [1,*], Chenxi Duan [2], Yang Yang [1] and Xiqi Wang [1]

[1] School of Remote Sensing and Information Engineering, Wuhan University, Wuhan 430079, China
[2] State Key Laboratory of Information Engineering in Surveying, Mapping, and Remote Sensing, Wuhan University, 430079, China
* Correspondence: lironui@whu.edu.cn (R.L.); syzheng@whu.edu.cn (S.Z.)

Abstract: In recent years, more and more researchers have gradually paid attention to Hyperspectral Image (HSI) classification. It is significant to implement researches on how to use HSI's sufficient spectral and spatial information to its fullest potential. To capture spectral and spatial features, we propose a Double-Branch Dual-Attention mechanism network (DBDA) for HSI classification in this paper. Two branches are designed to extract spectral and spatial features separately to reduce the interferences between these two kinds of features. What is more, because distinguishing characteristics exist in the two branches, two types of attention mechanisms are applied in two branches above separately, ensuring to exploit spectral and spatial features more discriminatively. Finally, the extracted features are fused for classification. A series of empirical studies have been conducted on four hyperspectral datasets, and the results show that the proposed method performs better than the state-of-the-art method.

Keywords: hyperspectral image classification; spectral-spatial feature fusion; channel-wise attention; spatial-wise attention

1. Introduction

Remote sensing image which can be characterized by the spatial resolution, the spectral resolution and the temporal resolution [1] has been researched thoroughly and generally in plentiful areas such as land-cover mapping [2], water monitoring [3] and anomaly detection [4]. Hyperspectral Image (HSI), a particular genre of remote sensing image, owns abundant information both on spectral and spatial aspects [5], and has been applied to many practical applications including vegetation cover monitoring [6], atmospheric environmental research [7], and change area detection [8], among others.

The essential task of HSI lies in supervised classification, and the classification of pixels is the most common technology used in these applications. However, 'curse of dimensionality' emergences when we intend to deal with the enormous spectral features, which makes conventional methods bleak and grim. Therefore, one of the essential cores in HSI classification is extracting the most discriminatory features from abundant spectral bands. Traditional pixel-wise HSI classification models mainly consist of two steps: feature engineering and classifier training, the former aims to extract the most discriminative bands by reducing the dimensionality and the latter refers to training general-purpose classifiers using these characteristic features.

Spectral-based models were adopted by researchers in the early study, such as support vector machines (SVM) [9], multinomial logistic regression [10, 11], and dynamic or random subspace [12, 13], which ignore the high spatial correlation and local consistency in HSI. Therefore, increasing spectral-spatial feature-based classification (SSFC) frameworks have been presented that take spatial information into account. For example, two types of low-level features, morphological profiles [14] and Gabor feature [15], were developed to explore the spatial information. Morphological kernel [16] and composite kernel [17] were also designed to exploit the spectral-spatial information. In [18], Fang L et al. proposed a superpixel-based strategy to utilize the spatial information within each extinction

© 2019 by the author(s). Distributed under a Creative Commons CC BY license.

profile (EP) adaptively. Thought the using of spatial information had provided improvements in performance, the high dependence on hand-crafted or shallow-based descriptors limits the applicability of these methods, especially in complex scenarios. One method may get excellent results on a dataset while obtaining terrible performance on another.

In the meanwhile, Deep Learning (DL) has been introduced in many computer vision tasks and has made significant breakthroughs, such as objection detection [19], natural language processing [20], and image classification [21]. As a specific genre of image classification tasks, HSI classification has influenced by the DL deeply and has obtained excellent performance. Stacked Autoencoders (SAE), Deep Autoencoder (DAE), Recursive Autoencoder (RAE), Deep Belief Networks (DBN), Convolutional Neural Networks (CNN), Recurrent Neural Networks (RNN), and Generative Adversarial Networks (GAN) et al. have been successively used in the areas of HSI classification.

In [22], Principle Component Analysis (PCA) was used to condense the size of the image, Stacked Autoencoders (SAE) was utilized to extract useful features, and logistic regression was applied to classify the HSI. Analogously, two sparse SAEs were used to extract spectral and spatial information, respectively, in [23], while the classifier was a linear SVM. A single spatial updated deep autoencoder (DAE) was adopted by Ma et al. [24] to extract spectral-spatial features, and a collaborative representation-based classification was used to handle the problem of the small-scale training set. Zhang et al. [25] extracted high-level features from the neighborhoods of the target pixel using a Recursive Autoencoder (RAE) and fused the neighboring spatial information by a new weighting scheme. Chen et al. [26] proposed a classification framework based on Restricted Boltzmann Machine (RBM) and Deep Belief Network (DBN).

A crucial weakness of the methods above is that they exploit the spatial features just in one dimension in that the limit of the input shape ruins the initial spatial structure. Moreover, the emergence of the convolutional neural network (CNN) renders a better solution. Makantasis et al. [27] encoded the spectral and spatial information by a CNN and classified the pixel via a Multi-Layer Perceptron. Zhao et al. [28] proposed a spectral-spatial feature-based classification (SSFC) framework in which a balanced local discriminant embedding algorithm was adopted to reduce the dimension, a CNN was introduced to explore the high-level features and a multiple-feature-based classifier was trained to classify the pixel. In [29], feature extraction (FE) method using CNN was put forward, and a deep FE model with a three-dimensional convolutional neural network (3D-CNN) was built to exploit the spectral and spatial characteristics. Similarly, Li et al. [30] extracted the spectral-spatial features via a 3D-CNN without any preprocessing or post-processing.

Inspired by the latest development of DL fields, some new methods could be seen in the literature. Mou et al. [31] proposed a Recurrent Neural Networks (RNN) framework for hyperspectral image classification in which hyperspectral pixels were analysed via the sequential perspective. As the severe absence of labeled samples in HSI, certain techniques were introduced successively, including Semi-Supervised Learning (SSL) [32], Generative Adversarial Network (GAN) [33] and Active Learning (AL) [34]. In [35], spectral-spatial Capsule Networks (CapsNets) was designed in order to reduce the complexity of the network and increase the accuracy of the classification. Have also been gotten noticed Self-pace learning [36], self-taught learning [37], and superpixels based methods [38] et al.

1.1. Inspiration

The emergence of the Residual Network (ResNet) [39] and the Dense Convolutional Network (DenseNet) [40] has conquered the notorious problem of vanishing and exploding gradients to a great extent, especially for the quite deep network. Inspired by the ResNet, a Spectral-Spatial Residual Network (SSRN) [41] was built by Zhong et al. in which a residual spectral block and a residual spatial block were designed to extract signatures consecutively. Wang et al. proposed a Fast Dense Spectral-Spatial Convolution (FDSSC) framework [42] based on SSRN. Fang designed a 3-D dense convolutional network with Spectral-wise Attention Mechanism (MSDN-SA) on the strength of DenseNet and attention mechanism [43].

Nevertheless, the common defect of SSRN and FDSSC is that the two frameworks take the extracted spectral features as the input of the extractor of spatial features, or in other words, the spectral extractor is in series with the spatial extractor. As the spectral features and spatial features are in the disparate realm, the spectral features might be devastated when extracting the spatial features. Moreover, MSDN-SA lacks spatial-wise attention.

Motivated by Convolutional Block Attention Module (CBAM) [44], an intuitive and practical attention module, Ma et al. proposed a Double-Branch Multi-Attention mechanism network (DBMA) [45] which consists of a spectral branch and a spatial branch. However, the generalization ability of the CBAM was prudently doubted by literature [46].

Recently, a more flexible and adaptive self-attention mechanism module named Dual Attention Network (DANet) [47] was put forward by Fu, which could integrate local features with their global dependencies to capture long-range contextual information, and leads to outstanding performance in the task of Scene Segmentation.

Motivated by the DANet and to handle the weakness of SSRN, FDSSC, and DBMA, we propose the Double-Branch Dual-Attention mechanism network (DBDA) for HSI classification. The spectral branch and spatial branch are designed parallelly, and the channel-wise attention mechanism and spatial-wise attention mechanism are built separately. The syncretic spectral-spatial feature is obtained by concatenating the output of two branches. To get the final classification result, a softmax classifier is adopted in the end. Codes will be made publicly available at https://github.com/lironui/Double-Branch-Dual-Attention-Mechanism-Network as soon as possible.

1.2. Contribution

The three significant contributions of this paper can be listed as follows:

- Based on densely connected and 3D-CNN, we proposed an end-to-end spectral-spatial convolution network named Double-Branch Dual-Attention mechanism network (DBDA), which enables to extract the features separately via spectral branch and spatial branch without any feature engineering. The extracted features of each branch are fused for classification.
- A more flexible and adaptive self-attention mechanism both on the channel-wise and spatial-wise is introduced compared with DBMA. The channel-wise attention is designed to focus on informative spectral characteristics while suppressing unserviceable spectral characteristics, and the spatial attention is built to concentrate on the informative areas in the input patches.
- Compared with other recently proposed frameworks, the DBDA achieves state-of-the-art classification accuracy in four datasets using limited training data with a fixed spatial size. Furthermore, the training time our proposed network is also less than the two compared deep-learning algorithms.

The rest of this paper is organized as follows: Section 2 expounds on the details of the proposed model. Section 3 introduces the datasets and experimental settings. Section 4 elaborates on the experiment results and analysis. Finally, a conclusion of the whole paper and the direction of our future research are presented in Section 5.

2. Proposed Framework

In this section, the framework of the DBDA will be expounded in detail, including the densely-connected structure, the channel-wise attention mechanism, and the spatial-wise attention mechanism. The graphical flowchart showed in Figure **Figure 1** summarizes our whole procedure step by step. In this framework, all labeled data are divided into a training set, a validation set, and a testing set. An HSI data set X is composed by N annotated pixels $\{x_1, x_2, \dots, x_n\} \in \mathbb{R}^{1\times1\times b}$ while the corresponding category label set is $Y = \{y_1, y_2, \dots, y_n\} \in \mathbb{R}^{1\times1\times c}$ where b and c represent the amounts of spectral bands and classes of land-cover severally. The data cube $Z = \{z_1, z_2, \dots, z_n\} \in \mathbb{R}^{p\times p\times b}$ is generated by the $p \times p$ neighborhoods centered on each pixel in X, which is taken to utilize the spectral and spatial characteristics adequately. Moreover, the p, i.e. patch size, is set as 9 in our framework. Then, the samples are divided into a training set Z_{train}, a validation set Z_{val} and a

Preprints (www.preprints.org) | NOT PEER-REVIEWED | Posted: 5 December 2019 doi:10.20944/preprints201912.0059.v1

testing set Z_{test}. Accordingly, their corresponding label vectors are divided into Y_{train}, Y_{val} and Y_{test}.

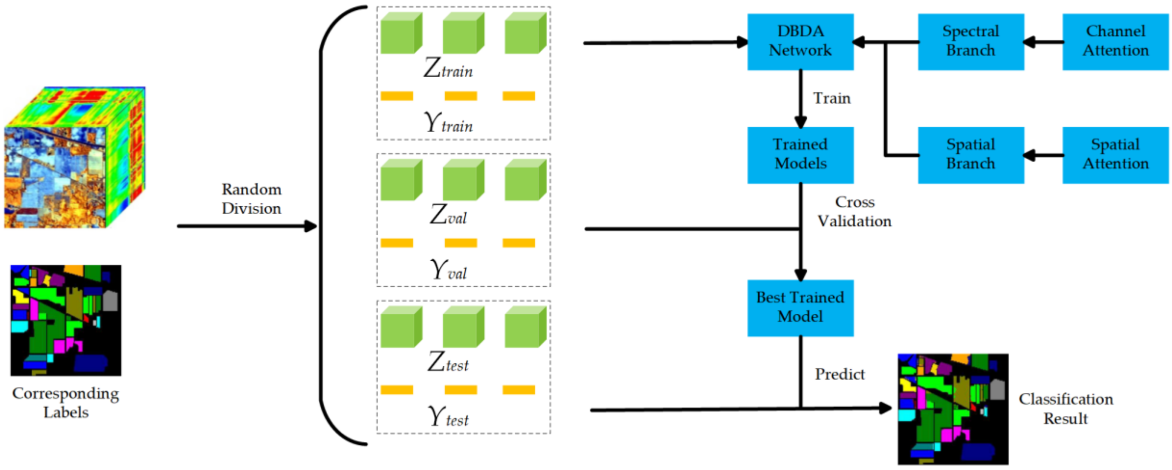

Figure 1. The procedure of the DBDA framework. The training set Z_{train} and corresponding labels vector Y_{train} are used to update the parameters. The validation set Z_{val} and corresponding labels vector Y_{val} are adopted to monitor the interim models and select the best-trained model. The test set Z_{test} and corresponding labels vector Y_{test} are chosen to verify the effectiveness of the trained model.

After the architecture of the model was constructed, and the hyperparameters of the network were configured, the training set is used to update the parameters for certain epochs. The backpropagating gradients are calculated by the cross-entropy objective function as:

$$C(\hat{y}, y) = \sum_{m=1}^{L} y_m \left(log \sum_{n=1}^{L} e^{\widehat{y_n}} - \widehat{y_m} \right) \tag{1}$$

where $\hat{y} = [\hat{y}_1, \hat{y}_2, \dots, \hat{y}_L]$ represents the predicted label vector by the model and $y = [y_1, y_1, \dots y_l]$ means the ground-truth label vector. The validation set is adopted to monitor the interim models and select the best-trained model. Finally, the test set is chosen to verify the effectiveness of the trained model.

2.1. Densely-Connected Structure

When it comes to DenseNet [40], we cannot dispense with ResNet [39]. Generally, a residual connection named skip connection is added to the tradition CNN model. As is shown in Figure

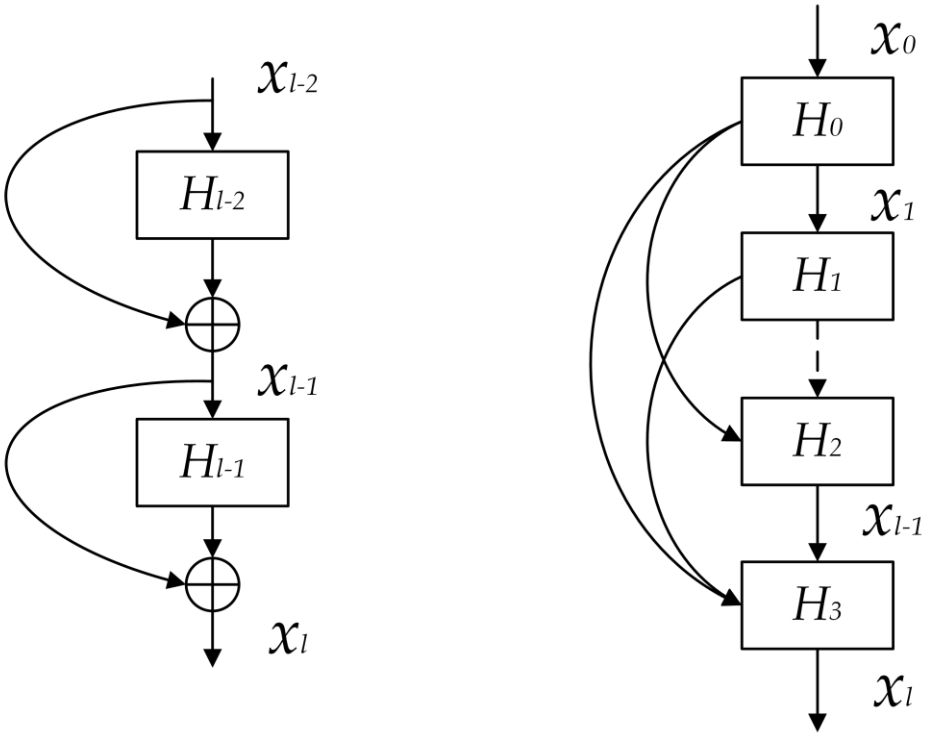

(a) Residual connection (b) Densely connection

Figure 2a, *H*, the abbreviation of the hidden block, is a module including specific convolutional layers, activation layers, and batch normalization layers. The existence of the skip connection, which can be seen as an identity mapping, enables the input to pass directly through the network. ResNet is designed out of modules named residual block, and the output of the *l-th* residual block can be calculated as:

$$x_l = H_l(x_{l-1}) + \ x_{l-1} \tag{2}$$

The residual mapping lets each stacked layer fit another mapping of $F(x) := H(x) - x$, so the original mapping *F(x)* is recast into $F(x) + x$ which makes the optimization of the network easier without any extra parameters.

To guarantee maximum information flow between each layer in the network, DensNet, which directly connects all layers with matching feature-map sizes, is built based on ResNet. Instead of combining features through summation like ResNet, DensNet combines features via concatenating them at the channel dimension. DenseNet is designed out of modules named dense block and transition layer, and the output of the *l*-th dense block can be computed as:

$$x_l = H_l[x_0, x_1, \dots, x_{l-1}] \tag{3}$$

in which H_l is a module including batch normalization, activation layers, and convolution layers, and $x_0, x_1, \dots, x_{l-1}$ are the feature maps of the preceding dense blocks. The transition layer, which does convolution and pooling, is adopted to control the dimension of feature maps. As is shown in Figure **Figure** 2b, DenseNet with *L* layers owns $L(L+1)/2$ direct connections in compared with *L* in traditional convolutional networks, which ensure the adequate flow of information.

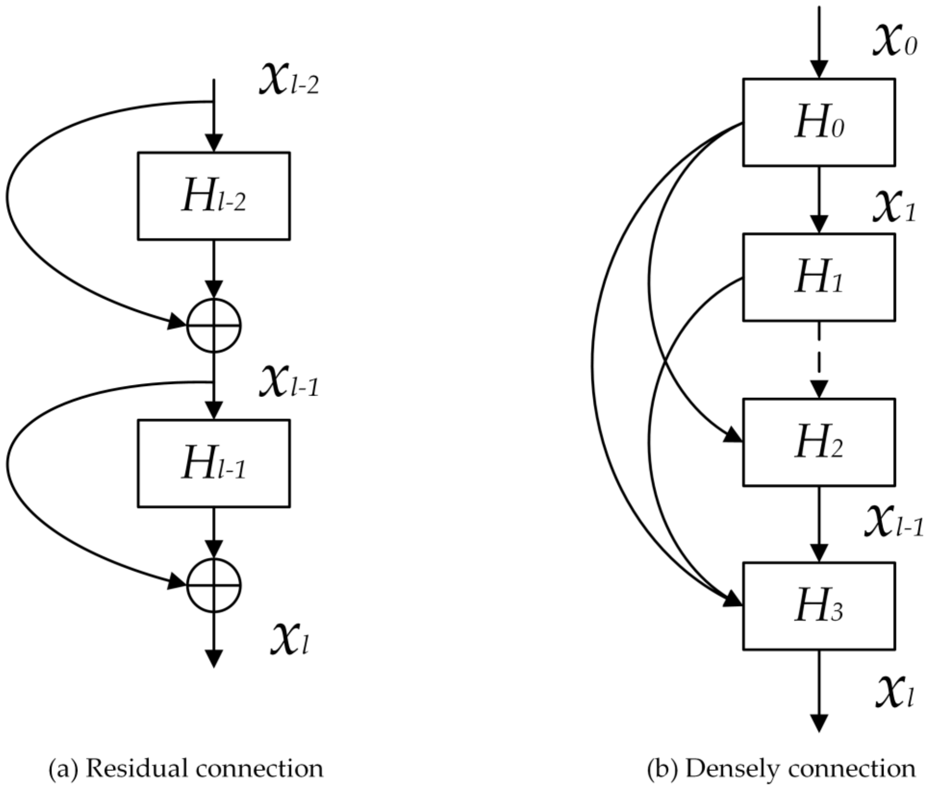

Figure 2. The architecture of Residual connection and Dense connection.

The structure of the dense block used in our framework can be seen in Figure **Figure 3**. Supposing the size of the input feature maps as $p \times p \times b$ with n channels, then the output feature maps of each composite convolution layer composed of k kernels in the shape of $1 \times 1 \times d$ are $p \times p \times b$ with k channels. However, as we know, dense connection concatenates feature maps at the channel dimension, so the number of channels increases linearly with the number of composite convolution layers. The channel's quantity of a dense block with m layers can be formulated as:

$$k_m = b + (m-1) \times k \tag{4}$$

where b is the channel's index of the input feature maps.

2.2. *The Measures Taken to Prevent Overfitting*

A large number of training parameters and the limited number of training sets lead to the tendency to overfit the seen data jointly. Next, we are going to elaborate on the measures taken to prevent overfitting.

The activation function we adopted is Mish [48], a self-regularized non-monotonic activation function, instead of the conventional ReLU [49]. The formula of the Mish is:

$$mish(x) = x \times tanh\big(softplus(x)\big) = x_i \times tanh\big(ln(1+e^x)\big) \tag{5}$$

where x represents the input of the activation. The comparison of Mish and ReLU can be seen in Figure **Figure 4**. Mish is lower bounded, and upper unbounded with a range $[\approx -0.31, \infty)$. The derivative of Mish is defined as:

$$f'(x) = \frac{e^x \omega}{\delta^2} \tag{6}$$

where $\omega = 4(x+1) + 4e^x + e^{3x} + e^x(4x+6)$ and $\delta = 2e^x + e^{2x} + 2$.

Preprints (www.preprints.org) | NOT PEER-REVIEWED | Posted: 5 December 2019 doi:10.20944/preprints201912.0059.v1

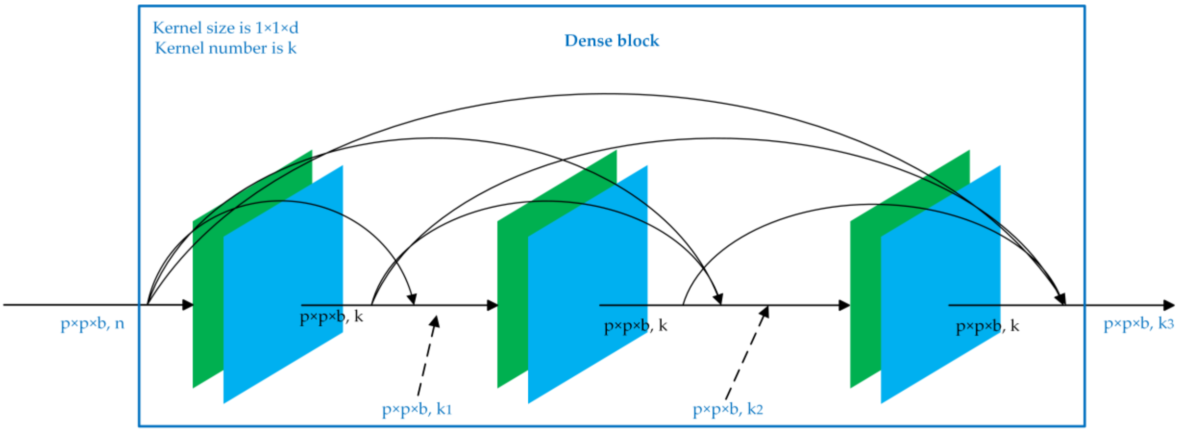

Figure 3. The architecture of dense connection.

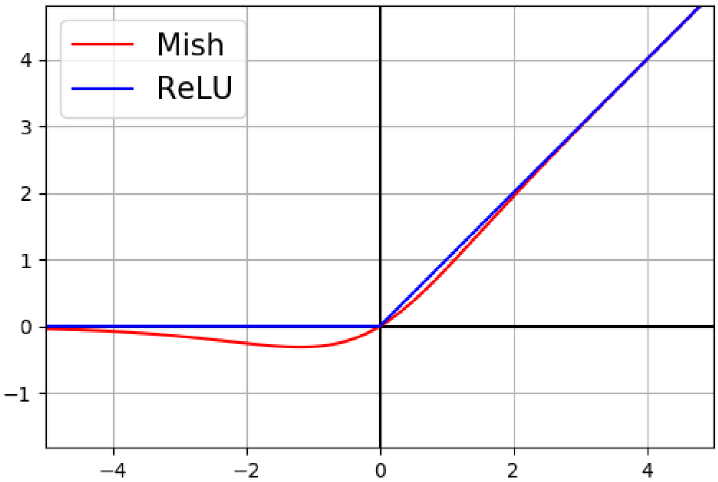

Figure 4. The comparison of the function graphs of Mish and ReLU.

As we know, the ReLU activation function defined as $ReLU(x) = max(0, x)$ is a piecewise linear function which prunes all the negative inputs. Moreover, the sparsity in the neural network is induced by this property on account of if the input is nonpositive, then the neuron is going to "die" and cannot be activated anymore, even though negative inputs might involve salutary information. On the contrary, slight negative inputs are preserved as negative outputs by Mish, which tradeoffs the input information and the network sparsity better.

A drop layer [50] is adopted between the last batch normalization layer and the global average pooling layer in the spectral branch and spatial branch severally. Dropout is a simple but effective technology to prevent overfitting by dropping out units (hidden or visible) on a given percentage p at the training phase. Moreover, the p is selected as 0.5 in our framework. The existence of dropout makes the presence of other units unreliable, which prevents co-adaptation between each unit.

Besides, two training skills, early stopping, and the dynamic learning rate are also introduced to our model. Early stopping means if the loss is no longer decreasing for a certain number of epochs (in our model, the number is 20), then we will stop the training process early to prevent overfitting and reduce the training time meanwhile. For the sake of dynamical learning rate, the cosine annealing [51] method is adopted to adjust the learning rate dynamically as the followed equation:

Preprints (www.preprints.org) | NOT PEER-REVIEWED | Posted: 5 December 2019 doi:10.20944/preprints201912.0059.v1

$$\eta_t = \eta_{min}^i + \frac{1}{2}\left(\eta_{max}^i - \eta_{min}^i\right)\left(1 + \cos\left(\frac{T_{cur}}{T_i}\pi\right)\right) \tag{7}$$

where η_t is the learning rate within the *i*-th run and $[\eta_{min}^i, \eta_{max}^i]$ is the range of the learning rate. T_{cur} accounts for the count of epochs that have been executed, and T_i controls the count of epochs that will be executed in a cycle of adjustment.

2.3. *Attention Mechanism*

Instead of processing a whole scenario across-the-board at once, human perception tends to pay attention selectively to portions of the visual space in order to acquire information when and where it is required and integrate information from various fixations over time to generate an internal representation of the scenario [52]. Inspired by above-mentioned percipience, the attention mechanism has been introduced in image categorization [53], and were later proved to be dominant in the areas including Image Caption [54], Text to Image Synthesis [55] and Scene Segmentation [47], et al. Obviously, diverse spectral channel and zones of different of the input patch make the discrepant contribution to extracting features. Therefore, the attention mechanism can be adapted to focus on the most compelling part and compress the inconsequential region's weight.

Within our framework, feature maps generated by anterior dense spectral block and dense spatial block are fed into spectral attention module and spatial attention module separately. By spectral attention module, the weight of each spectrum is adjusted to highlight the informative channel. Likewise, the spatial attention module makes discriminative areas at spatial dimension prominent.

In DANet [47], after feeding the features into the spatial attention module, features of spatial long-range contextual information are generated by three steps. In the first step, a spatial attention matrix is computed, which models the spatial relationship between any two pixels of the features. Next, a matrix multiplication between the original features and the attention matrix is performed. Finally, an element-wise sum operation on the original features and the multiplied resulting matrix is executed to obtain the final representation, which reflects long-range contexts. Similarly, long-range contextual information in the channel dimension is extracted by a spectral attention module, meanwhile just like the spatial attention module expects for the first step, in which the channel attention matrix is calculated in channel dimension. Next, the two modules would be introduced in detail.

2.3.1. Spatial Attention Module

Long-range contextual information is captured to obtain discriminant feature representations by the spatial attention module. Against that, what features generated by conventional fully convolutional networks (FCNs) considers merely is the local connection.

As illustrated in Figure **Figure 5**a, given a local feature $\boldsymbol{A} \in \mathbb{R}^{c \times p \times p}$, two convolution layers are adopted to generate new feature maps **B** and **C** severally where $\{\boldsymbol{B}, \boldsymbol{C}\} \in \mathbb{R}^{c \times p \times p}$ (Note: Generally, the height and width of the input feature maps are unequal values, but overall feature maps of our framework are square in that we take the same patch size on the two dimensions to generate the original data cube). Next, **B** and **C** are reshaped into $\mathbb{R}^{c \times n}$ where $n = p \times p$ is the count of pixels. Then a matrix multiplication is executed between **B** and **C**, and a softmax layer is attached subsequently to compute the spatial attention map $\boldsymbol{S} \in \mathbb{R}^{n \times n}$:

$$s_{ji} = \frac{exp(B_i \times C_j)}{\sum_{i=1}^{N} exp(B_i \times C_j)} \tag{8}$$

where s_{ji} measures the *i*-th position's impact on the *j*-th position. The more similar feature representations of the two positions are, the stronger the correlation between them is.

Meanwhile, the initial input feature **A** is fed into a convolution layer to obtain a new feature map $\boldsymbol{D} \in \mathbb{R}^{c \times p \times p}$ which is reshaped into $\mathbb{R}^{c \times n}$ whereafter. Then a matrix multiplication is performed between **D** and $\mathbf{S^T}$, and the result is reshaped into $\mathbb{R}^{c \times p \times p}$ as:

Preprints (www.preprints.org) | NOT PEER-REVIEWED | Posted: 5 December 2019 doi:10.20944/preprints201912.0059.v1

$$E_j = \alpha \sum_{i=1}^{N} (s_{ji} D_j) + A_j \tag{9}$$

where α is initialized as zero and can be learned to assign more weight gradually. By Equation 9, it can be inferred that all positions and original features are added with a certain weight to get the resulting feature $\boldsymbol{E} \in \mathbb{R}^{c \times p \times p}$. Therefore, the global contextual view and contexts aggregated selectively are generated within the spatial attention map.

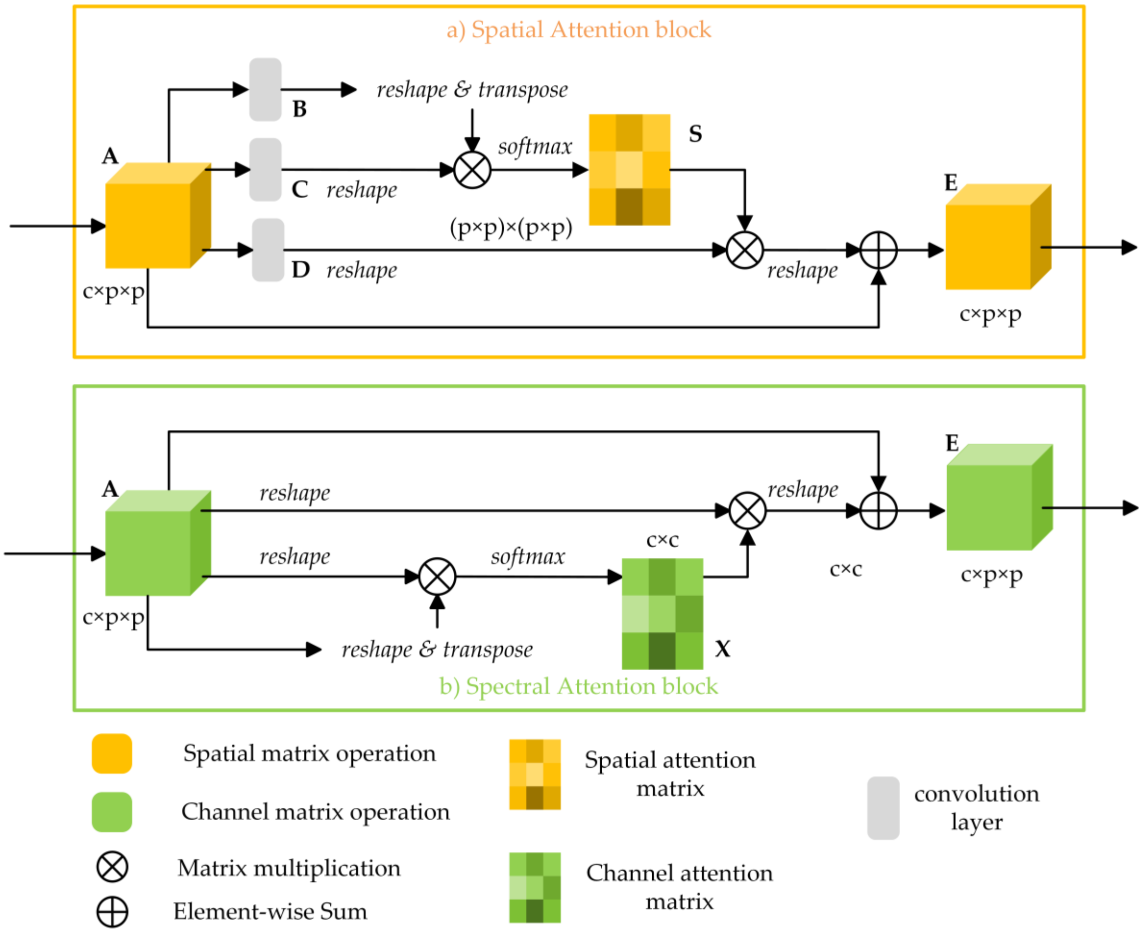

Figure 5. The details of the Spatial Attention Block and Spectral Attention Block.

2.3.2. Spectral Attention Module

In order to enhance interdependent feature maps, a spectral attention module is built to explicitly model interdependencies between spectral channels.

As illustrated in Figure **Figure 5**b, the channel attention map $\boldsymbol{X} \in \mathbb{R}^{c \times c}$ is computed from the initial input $\boldsymbol{A} \in \mathbb{R}^{c \times p \times p}$ directly. Concretely, a matrix multiplication between **A** and $\mathbf{A}^{\mathbf{T}}$ is operated firstly, and a softmax layer is connected to obtain the channel attention map $\boldsymbol{X} \in \mathbb{R}^{c \times c}$ by:

$$x_{ji} = \frac{exp(A_i \times A_j)}{\sum_{i=1}^{C} exp(A_i \times A_j)} \tag{10}$$

in which x_{ji} measures the i-th channel's impact on the j-th channel similarly. Then, a matrix multiplication between $\mathbf{X}^{\mathbf{T}}$ and **A** is attached, and the result is reshaped into $\mathbb{R}^{c \times p \times p}$. Finally, the reshaped result is weighted by a scale parameter β, and an element-wise sum operation with the input **A** to obtain the final spectral attention map $\boldsymbol{E} \in \mathbb{R}^{c \times p \times p}$:

$$E_j = \beta \sum_{i=1}^{C} (x_{ji} A_j) + A_j \tag{11}$$

Preprints (www.preprints.org) | NOT PEER-REVIEWED | Posted: 5 December 2019 doi:10.20944/preprints201912.0059.v1

where β is initialized as zero and can be learned gradually. Similarly, the final map **E** is obtained by the weighted sum of all channels' feature, which can describe the long-range dependencies and boost the discriminability about features.

2.4. *The Structure of the DBDA network.*

The whole structure of the DBDA network can be seen in Figure **Figure 6**, and then we will elaborate on the whole process in detail.

2.4.1. Spectral Branch with Channel Attention Block

Just taking the Indian Pines dataset as an example, and the input patch size is set to $9 \times 9 \times 200$. In the Spectral Branch, a 3D convolutional layer with 24 channels whose kernel size is $1 \times 1 \times 7$ is used, and the stride is set to $(1,1,2)$ that can compress the count of channels. So, we can get the feature maps in the shape of $(9 \times 9 \times 97{,}24)$. Then, the dense spectral block combined by three convolutional layers with a batch normalization layer is attached. And each convolutional layer has 12 channels in the shape of $1 \times 1 \times 7$, and the stride is set to $(1,1,1)$. Calculated by Equation (4), we can obtain the feature maps with 60 channels. After traversing the last 3D convolutional layer in the shape of $(1 \times 1 \times 97{,}60)$, a $(9 \times 9 \times 1{,}60)$ feature map is generated. Due to the 60 channels make different contributions to the classification, a channel attention block, as illustrated in Figure **Figure 5**b and expatiated in Section 2.3.2, is adopted, which reinforces the informative channels and whittle informative-lacking channels. After obtaining the weighted spectral feature maps, a batch normalization layer and a drop layer are applied to enhance the numerical stability and vanquish the overfitting. Finally, we can gain a spectral feature with a size of 1×60 via a Global Average Pooling layer. The details of the structure can be seen in Table **Table 1**.

Table 1. The network structure of Spectral Branch.

Layer name	Kernel Size	Output Size
Input	-	$(9 \times 9 \times 200)$
Conv	$(1\times 1 \times 7)$	$(9 \times 9 \times 97{,}24)$
BN-Mish-Conv	$(1\times 1 \times 7)$	$(9 \times 9 \times 97{,}12)$
Concatenate	-	$(9 \times 9 \times 97{,}36)$
BN-Mish-Conv	$(1\times 1 \times 7)$	$(9 \times 9 \times 97{,}12)$
Concatenate	-	$(9 \times 9 \times 97{,}48)$
BN-Mish-Conv	$(1\times 1 \times 7)$	$(9 \times 9 \times 97{,}12)$
Concatenate	-	$(9 \times 9 \times 97{,}60)$
BN-Mish-Conv	$(1\times 1 \times 97)$	$(9 \times 9 \times 1{,}60)$
Channel Attention Block	-	$(9 \times 9 \times 1{,}60)$
BN-Drop-GlobalAveragePooling	-	(1×60)

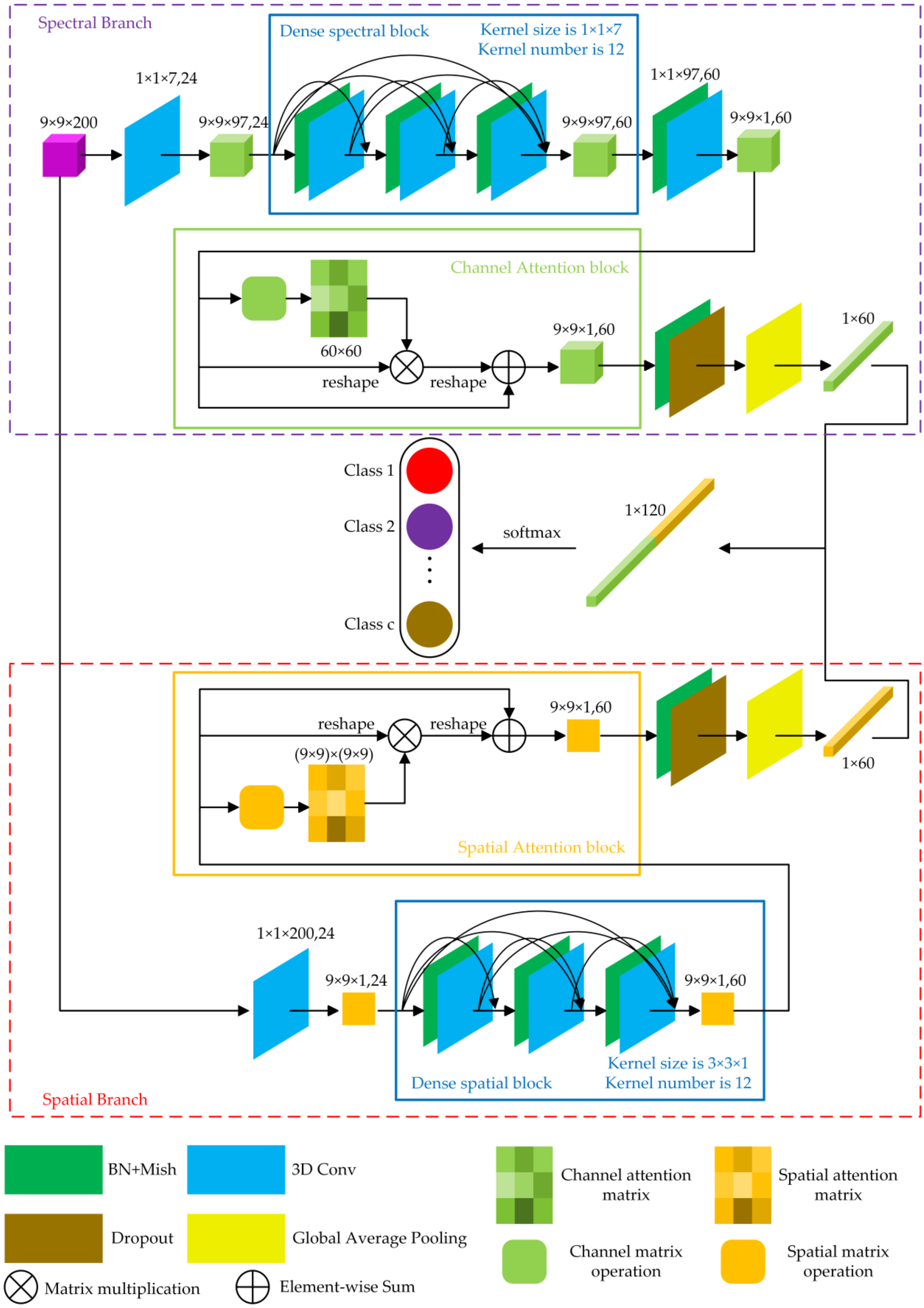

Figure 6. The structure of the DBDA network. The top branch, Spectral Branch composed of the dense spectral block and channel attention block, is designed to capture spectral features. The bottom branch, Spatial Branch constituted by dense spatial block, and spatial attention block is designed to extract spatial features.

Preprints (www.preprints.org) | NOT PEER-REVIEWED | Posted: 5 December 2019 doi:10.20944/preprints201912.0059.v1

2.4.2. Spatial Branch with Spatial Attention Block

Meanwhile, the input data in the shape of $9 \times 9 \times 200$ are delivered to the Spatial Branch, and the initial 3D convolutional layer's size is set to $1 \times 1 \times 200$, which can eliminate spectral channels. After that, we can obtain feature maps in the shape of $(9 \times 9 \times 1{,}24)$. Analogously, the dense spectral block combined by three convolutional layers with a batch normalization layer is attached. And each convolutional layer has 12 channels in the shape of $3 \times 3 \times 1$, and the stride is set to $(1{,}1{,}1)$. Next, the extracted feature maps with the size of $(9 \times 9 \times 1{,}60)$ are fed into the spatial attention block, as illustrated in Figure **Figure 5**a and expound in Section 2.3.1, in which the coefficient of each pixel is weighed to get a more discriminative spatial feature. After capturing the weighted spatial feature maps, a batch normalization layer and a drop layer are applied to heighten the numerical stability and defeat the overfitting. Finally, we can gain a spatial feature with a size of 1×60 via a Global Average Pooling layer. The details of the structure can be seen in Table **Table 2**.

2.4.3. Spectral-Spatial Fusion for Classification

The spectral feature and spatial feature are obtained by the Spectral Branch and Spatial Branch severally. Then, we perform a concatenation between two features for classification. Moreover, the reason why the concatenation is applied instead of add operation is that the spectral feature and spatial feature are in the disparate domain, but the add operation will mingle spectral and spatial features. In the end, the conclusive classification result is obtained via the fully connected layer and softmax activation.

For other datasets, network implementation details are executed in the same way, and the only difference is the number of bands.

Table 2. The network structure of the Spatial Branch.

Layer name	**Kernel Size**	**Output Size**
Input	-	$(9 \times 9 \times 200)$
Conv	$(1\times 1 \times 200)$	$(9 \times 9 \times 1{,}24)$
BN-Mish-Conv	$(3\times 3 \times 1)$	$(9 \times 9 \times 1{,}12)$
Concatenate	-	$(9 \times 9 \times 1{,}36)$
BN-Mish-Conv	$(3\times 3 \times 1)$	$(9 \times 9 \times 1{,}12)$
Concatenate	-	$(9 \times 9 \times 1{,}48)$
BN-Mish-Conv	$(3\times 3 \times 1)$	$(9 \times 9 \times 1{,}12)$
Concatenate	-	$(9 \times 9 \times 1{,}60)$
Channel Attention Block	-	$(9 \times 9 \times 1{,}60)$
BN-Drop-GlobalAveragePooling	-	(1×60)

3. Datasets Introduction and Experimental Setting

3.1. Datasets Introduction

In the experiments, four widely used HSI datasets, the Indian Pines (IP) dataset, the Pavia University (UP) dataset, the Salinas Valley (SV) dataset, and the Botswana dataset (BS), are employed to measure the accuracy and efficiency of the proposed model. Three quantitative metrics, overall accuracy (OA), average accuracy (AA), and Kappa coefficient (K), are used to assess the performance. OA denotes the proportion of correct classifications to the total pixels to be classified. AA refers to the average accuracy of all categories. Kappa coefficients can be used to verify the consistency and can also be used to measure accuracy. The higher the three metric values are, the better the classification consequence is.

Indian Pines (IP): The Indian Pines dataset was gathered by Airborne Visible/Infrared Imaging Spectrometer (AVIRIS) sensor in North-western Indiana, composed of 200 spectral bands in the wavelength range of 0.4 um to 2.5 um and 16 land cover classes. IP consists of 145×145 pixels, and the resolution is 20 m/pixel.

Pavia University (UP): The Pavia University dataset was acquired by the reflective optics imaging spectrometer (ROSIS-3) sensor from the University of Pavia, northern Italy, composed of 103 spectral bands in the wavelength range of 0.43 um to 0.86 um and nine land cover classes. UP consists of 610×340 pixels, and the resolution is 1.3 m/pixel.

Salinas Valley (SV): The Salinas Valley dataset was collected by the AVIRIS sensor from Salinas Valley, CA, USA, composed of 204 spectral bands in the wavelength range of 0.4 um to 2.5 um and 16 land cover classes. SV consists of 512×217 pixels, and the resolution is 3.7 m/pixel.

Botswana (BS): The Botswana dataset was captured by the NASA EO-1 satellite over the Okavango Delta, Botswana, composed of 145 spectral bands in the wavelength range of 0.4 um to 2.5 um and 14 land cover classes. BS consists of 1476×256 pixels, and the resolution is 30 m/pixel.

3.2. Experimental Setting

In our experiment, to evaluate the effectiveness of DBDA, we compared the proposed framework to other deep-learning-based classifier CDCNN [56], SSRN [41], FDSSC [42], and the state-of-the-art Double-Branch Multi-Attention Mechanism Network (DBMA) [45]. Furthermore, a conventional classifier, the SVM with RBF kernel [57], is also taken into comparison. The training time and testing time results were measured via the same computer configured with 32 GB of memory and an NVIDIA GeForce RTX 2080Ti GPU. All deep-learning-based classifiers were implemented with PyTorch, and SVM was implemented with sklearn. Then, a brief introduction to the above methods will be given separately.

Table 3. The number of training, validation, and test samples in the IP dataset.

Order	Class	Total number	Train	Val	Test
1	Alfalfa	46	3	3	40
2	Corn-notill	1428	42	42	1344
3	Corn-mintill	830	24	24	782
4	Corn	237	7	7	223
5	Grass-pasture	483	14	14	455
6	Grass-trees	730	21	21	688
7	Grass-pasture-mowed	28	3	3	22
8	Hay-windrowed	478	14	14	450
9	Oats	20	3	3	14
10	Soybean-notill	972	29	29	914
11	Soybean-mintill	2455	73	73	2309
12	Soybean-clean	593	17	17	559
13	Wheat	205	6	6	193
14	Woods	1265	37	37	1191
15	Buildings-Grass-Trees-Drives	386	11	11	364
16	Stone-Steel-Towers	93	3	3	87
	Total	10,249	307	307	9635

Table 4. The number of training, validation, and test samples in the UP dataset.

Order	Class	Total number	Train	Val	Test
1	Asphalt	6631	33	33	6565
2	Meadows	18,649	93	93	18463
3	Gravel	2099	10	10	2079
4	Trees	3064	15	15	3034
5	Painted metal sheets	1345	6	6	1333
6	Bare Soil	5029	25	25	4979
7	Bitumen	1330	6	6	1318
8	Self-Blocking Bricks	3682	18	18	3646

9	Shadows	947	4	4	939
	Total	42,776	210	210	42356

Table 5. The number of training, validation, and test samples in the SV dataset.

Order	Class	Total number	Train	Val	Test
1	Brocoli-green-weeds-1	2009	10	10	1989
2	Brocoli-green-weeds-2	3726	18	18	3690
3	Fallow	1976	9	9	1958
4	Fallow-rough-plow	1394	6	6	1382
5	Fallow-smooth	2678	13	13	2652
6	Stubble	3959	19	19	3921
7	Celery	3579	17	17	3545
8	Grapes-untrained	11,271	56	56	11159
9	Soil-vinyard-develop	6203	31	31	6141
10	Corn-senesced-green-weeds	3278	16	16	3246
11	Lettuce-romaine-4wk	1068	5	5	1058
12	Lettuce-romaine-5wk	1927	9	94	1824
13	Lettuce-romaine-6wk	916	4	4	908
14	Lettuce-romaine-7wk	1070	5	5	1060
15	Vinyard-untrained	7268	36	36	7196
16	Vinyard-vertical-trellis	1807	9	9	1789
	Total	54,129	263	263	53603

Table 6. The number of training, validation, and test samples in the BS dataset.

Order	Class	Total number	Train	Val	Test
1	Water	270	3	3	264
2	Hippo grass	101	2	2	97
3	Floodplain grasses1	251	3	3	245
4	Floodplain grasses2	215	3	3	209
5	Reeds1	269	3	3	263
6	Riparian	269	3	3	263
7	Fierscar2	259	3	3	253
8	Island interior	203	3	3	197
9	Acacia woodlands	314	4	4	306
10	Acacia shrublands	248	3	3	242
11	Acacia grasslands	305	4	4	297
12	Short mopane	181	2	2	177
13	Mixed mopane	268	3	3	262
14	Exposed soils	95	1	1	93
	Total	3248	40	40	3168

SVM: For SVM, all spectral bands are fed into SVM with a radial basis function (RBF) kernel.

CDCNN: The architecture of the CDCNN is rendered in [56], which is based on 2D CNN and ResNet. The input data consists of $5 \times 5 \times L$ neighbors of each pixel, where L represents the number of spectral bands.

SSRN: The architecture of the SSRN is expounded in [41], which is based on 3D CNN and ResNet. The input data is composed of $7 \times 7 \times L$ neighbors of each pixel.

FDSSC: The architecture of the FDSSC is elaborated in [42], which is based on 3D CNN and DenseNet. The size of the input is $9 \times 9 \times L$.

DBMA: The architecture of the DBMA is set out in [42], which is based on 3D CNN, DenseNet, and an attention mechanism. The input patch size is set to $7 \times 7 \times L$.

For all we know, deep learning algorithms are data-driven, which rely on teeming labeled training samples severely. The more data fed in training usually yields the higher test accuracy with more time consumption and computation complexity followed. For the IP dataset, we choose 3% training samples and 3% validation samples. As the samples are enough for each class of UP and SV, we select 0.5% training samples and 0.5% validation samples. Furthermore, for BS, the proportion of training samples and validation samples is set to 1.2%. (The reason why decimal appears is that the number of samples in BS is sparse, so we set ratio as 1% with an operation of the ceiling.) To the best of authors' knowledge, it is the first time that so few samples are adopted to train and validate the model hitherto. For example, 16%, 20%, 10 %, and 5% of the IP samples are chosen for training CDCNN, SSRN, FDSSC, and DBMA in their papers, respectively.

For CDCNN, SSRN, FDSSC, DBMA, and our proposed method, the batch size is set to 16, and the optimizer is Adam with a learning rate of 0.0005 and 200 epochs as the upper limit. The early stopping strategy is adopted for each model, which means if the loss in the validation set does not reduce for 20 epochs, the training stage will be terminated.

4. Experimental Results

In our experiment, SVM with RBF kernel [57], CDCNN [56], SSRN [41], FDSSC [42] and DBMA [45] were compared with our proposed framework at the same computing platform configured with 32 GB of memory and an NVIDIA GeForce RTX 2080Ti GPU. Furthermore, all deep-learning-based classifiers were implemented with PyTorch.

4.1. Classification Maps and Results

The results of each dataset are demonstrated in Table **Table 7**-**Table 10**, and the best class-specific accuracy is in bold. Figure **Figure 7**-**Figure 10** displays the classification maps of each method. As can be seen both in the figures and tables, our method obtains the state-of-the-art results on four datasets.

Within the scope of deep-learning-based methods, our experiments show that the proposed DBDA framework is dramatically superior to the CDCNN, SSRN, FDSSC, and DBMA, and balances the accuracy and efficiency better. SVM and CDCNN perform poorly at most of the datasets. Although the DBMA has state-of-the-art accuracy claimed in [45], the DBMA presents inferior performance than the FDSSC on the IP and UP dataset, which may owe to finite training samples making overfitting become a significant influencing factor. For the IP dataset, UP dataset, SV dataset, and BS dataset, the proposed model obtains 2.23%, 2.75%, 2.07%, and 2.81% ameliorations compared with the DBMA.

What is more, the classification accuracies gained by proposed methods for each class in the IP, UP, SV, and BS dataset are not less than 82%. Taking the class 7 in the IP dataset as an example, which has only three training samples, our method performs well and obtains an acceptable consequence 92.59%, while the results of other methods (SVM: 56.10%, CDCNN: 0.00%, SSRN: 0.00%, FDSSC: 73.53%, and DBMA: 40.00%) are unpardonable seemingly.

Table 7. Class-specific results for the IP dataset using 3% training samples.

Class	Color	SVM	CDCNN	SSRN	FDSSC	DBMA	Proposed
1		24.24	0.00	**100.0**	85.42	93.48	**100.0**
2		58.10	62.36	89.14	97.20	91.15	88.49
3		64.37	57.00	77.49	94.45	99.58	97.12
4		37.07	37.50	88.95	**100.0**	98.57	**100.0**
5		87.67	88.16	96.48	**100.0**	97.45	**100.0**
6		84.02	79.63	98.15	**100.0**	95.66	`97.18
7		56.10	0.00	0.00	73.53	40.00	92.59
8		89.62	84.02	84.54	99.78	**100.0**	99.78
9		21.21	0.00	0.00	**100.0**	38.10	**100.0**
10		65.89	37.50	92.07	89.25	85.98	89.87

11		62.32	53.25	90.89	93.97	94.39	99.33
12		52.40	42.96	84.19	95.41	89.92	98.50
13		94.30	49.47	98.47	**100.0**	99.48	96.02
14		90.15	76.71	94.56	93.14	92.81	93.22
15		63.96	62.60	84.11	90.61	89.66	96.99
16		98.46	83.70	91.40	96.55	96.55	94.38
OA		69.41	62.32	89.81	94.87	93.15	95.38
AA		65.62	50.93	79.40	94.33	87.67	96.47
kappa		0.6472	0.5593	0.8839	0.9414	0.9219	0.9474

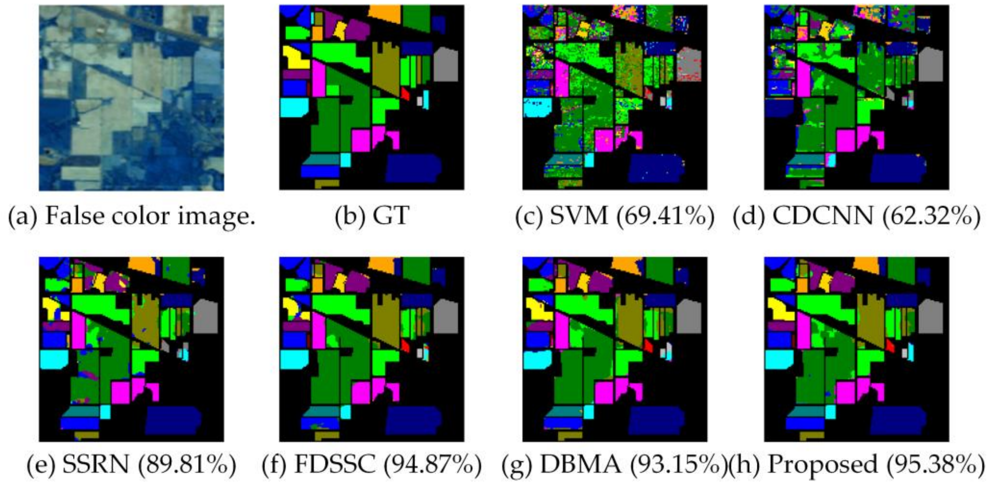

Figure 7. Classification maps of the IP dataset with 3% training samples. (a) False-color image. (b) ground-truth (GT). (c)–(h) The classification maps using different methods.

Table 8. Class-specific results for the UP dataset using 0.5% training samples.

Class	Color	SVM	CDCNN	SSRN	FDSSC	DBMA	Proposed
1		82.87	85.74	99.15	99.43	91.66	89.03
2		88.07	94.45	98.06	98.57	97.65	98.32
3		70.84	32.59	96.64	**100.0**	99.78	98.70
4		95.61	97.46	99.86	99.20	97.66	98.42
5		92.24	99.10	99.85	99.92	99.63	99.78
6		76.98	80.88	96.88	98.17	82.52	98.57
7		68.98	88.83	73.24	93.64	87.04	95.84
8		71.14	66.19	82.36	74.61	88.55	89.47
9		99.89	96.01	**100.0**	99.79	95.51	99.89
OA		84.29	87.70	95.59	95.88	93.25	96.00
AA		82.96	82.36	94.01	95.93	93.00	96.45
kappa		0.7883	0.8359	0.9415	0.9453	0.9108	0.9467

Preprints (www.preprints.org) | NOT PEER-REVIEWED | Posted: 5 December 2019 doi:10.20944/preprints201912.0059.v1

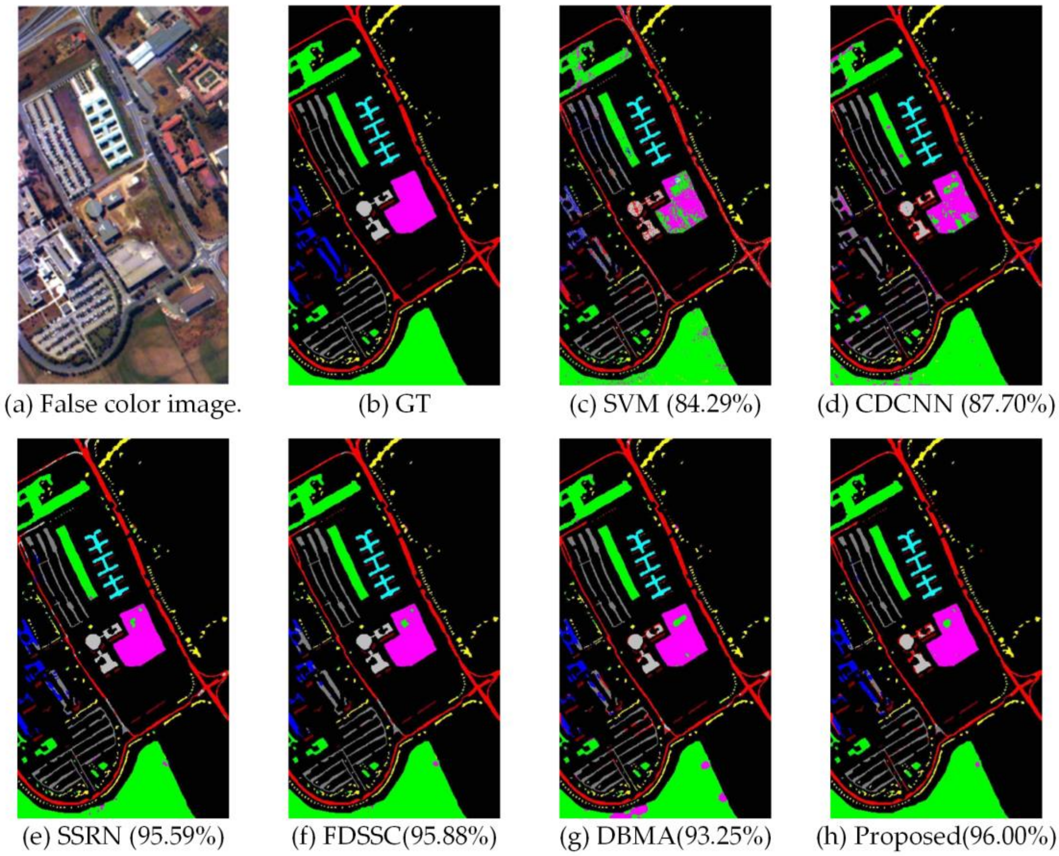

Figure 8. Classification maps of the UP dataset with 0.5% training samples. (a) False-color image. (b) ground-truth (GT). (c)–(h) The classification maps using different methods.

Table 9. Class-specific results for the SV dataset using 0.5% training samples.

Class	Color	SVM	CDCNN	SSRN	FDSSC	DBMA	Proposed
1		99.85	0.00	**100.0**	**100.0**	**100.0**	**100.0**
2		98.95	64.82	**100.0**	**100.0**	99.51	99.17
3		89.88	94.69	89.72	99.44	98.92	97.74
4		97.30	82.99	94.85	98.57	96.39	95.95
5		93.56	98.24	99.39	99.87	96.39	99.29
6		99.89	96.51	99.95	99.97	99.17	99.92
7		91.33	95.98	99.75	99.75	96.80	99.83
8		74.73	88.23	88.60	99.60	95.60	95.97
9		97.69	99.26	98.48	99.69	99.22	99.37
10		90.01	67.39	98.81	99.02	96.20	96.72
11		75.92	72.03	93.30	92.77	82.29	93.72
12		95.19	75.49	99.95	99.64	99.17	**100.0**
13		94.87	95.71	**100.0**	**100.0**	98.91	**100.0**
14		89.26	94.92	97.86	98.05	98.22	96.89
15		75.86	51.88	89.96	74.58	84.71	93.42
16		99.03	99.62	**100.0**	**100.0**	**100.0**	**100.0**
OA		88.09	77.79	94.72	94.99	95.44	97.51
AA		91.45	79.86	96.66	97.56	96.34	98.00
kappa		0.8671	0.7547	0.9412	0.9444	0.9493	0.9723

Preprints (www.preprints.org) | NOT PEER-REVIEWED | Posted: 5 December 2019 doi:10.20944/preprints201912.0059.v1

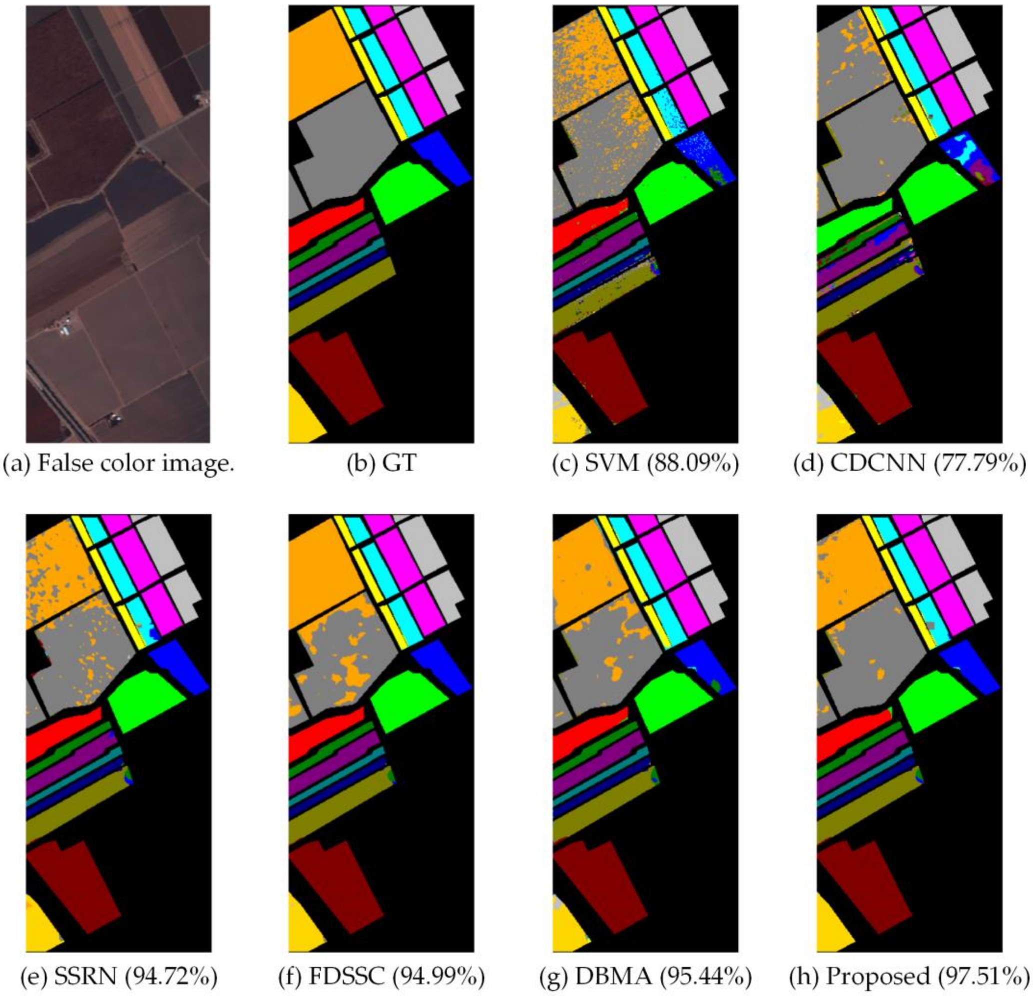

Figure 9. Classification maps of the SV dataset with 0.5% training samples. (a) False-color image. (b) ground-truth (GT). (c)–(h) The classification maps using different methods.

Table 10. Class-specific results for the BS dataset using 1.2% training samples.

Class	Color	SVM	CDCNN	SSRN	FDSSC	DBMA	Proposed
1		**100.0**	94.60	94.95	97.41	97.77	95.64
2		97.56	68.64	**100.0**	98.95	88.89	98.99
3		86.35	81.11	91.42	**100.0**	**100.0**	**100.0**
4		63.51	65.45	97.34	93.03	92.51	91.30
5		84.33	89.10	92.42	80.74	93.51	95.58
6		61.27	69.28	66.39	84.93	68.94	82.23
7		82.09	80.07	**100.0**	84.62	**100.0**	**100.0**
8		63.46	89.36	**100.0**	93.36	96.10	95.63
9		63.53	55.53	90.75	88.44	85.15	96.50
10		65.74	81.69	86.83	99.59	97.60	98.79
11		93.91	92.48	**100.0**	99.67	99.66	99.67
12		90.70	90.91	**100.0**	**100.0**	97.79	**100.0**
13		73.62	88.59	94.83	81.59	**100.0**	**100.0**
14		92.98	**100.0**	**100.0**	**100.0**	**100.0**	**100.0**
OA		77.21	80.90	91.89	91.57	93.43	96.24
AA		79.93	81.92	93.92	93.02	94.14	96.74
kappa		0.7532	0.7930	0.9121	0.9086	0.9.89	0.9593

Preprints (www.preprints.org) | NOT PEER-REVIEWED | Posted: 5 December 2019 doi:10.20944/preprints201912.0059.v1

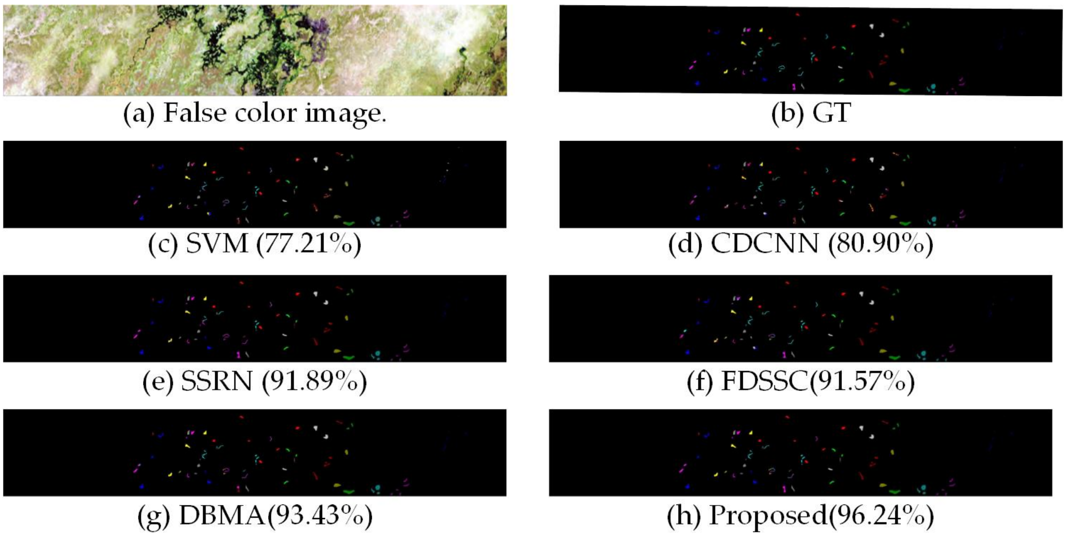

Figure 10. Classification maps of the BS dataset with 1.2% training samples. (a) False-color image. (b) ground-truth (GT). (c)–(h) The classification maps using different methods.

4.2. Investigation on Running Time

Tables **Table 11**-**Table 14** list the running time of the six methods on the IP, UP, SV, and BS datasets, respectively. From the tables above, we can see that the SVM-based method and 2D-CNN-based method consume less time than 3D-CNN-based methods; the latter means larger input size and more parameters generally. For our method, it spends less training time less than FDSSC and DBMA and obtains better performance.

Table 11. Training and testing time of different methods on the IP datasets.

Dataset	**Method**	**Training Times (s)**	**Test Times (s)**
Indian Pines	SVM	20.10	0.66
	CDCNN	11.13	1.54
	SSRN	46.03	2.71
	FDSSC	105.05	4.86
	DBMA	94.69	6.35
	Proposed	69.83	5.60

Table 12. Training and testing time of different methods on the UP datasets.

Dataset	Method	Training Times (s)	Test Times (s)
Pavia University	SVM	3.38	2.29
	CDCNN	10.26	4.92
	SSRN	17.71	6.41
	FDSSC	31.70	10.65
	DBMA	21.48	14.67
	Proposed	18.46	13.32

Table 13. Training and testing time of different methods on the SV datasets.

Dataset	**Method**	**Training Times (s)**	**Test Times (s)**
Salinas	SVM	9.35	3.89
	CDCNN	9.82	6.14
	SSRN	73.75	13.99
	FDSSC	99.91	25.57
	DBMA	105.30	31.82

Preprints (www.preprints.org) | NOT PEER-REVIEWED | Posted: 5 December 2019 doi:10.20944/preprints201912.0059.v1

	Proposed	71.18	23.93

Table 14. Training and testing time of different methods on the BS datasets.

Dataset	Method	Training Times (s)	Test Times (s)
Botswana	SVM	0.93	0.15
	CDCNN	11.10	1.33
	SSRN	8.87	1.37
	FDSSC	17.84	1.45
	DBMA	13.67	2.04
	Proposed	17.19	1.90

4.3. Investigation on the Number of Training Samples

As we mentioned, deep learning is a genre of data-driven algorithms, depending on superb annotated data. In this part, the performance with different amount of training samples would be investigated.

Figure **Figure 11** shows the experiment results. For IP dataset and BS dataset, 0.5%, 1%, 3%, 5% and 10% of samples are adopted as training set. For UP dataset and SV dataset, 0.1%, 0.5%, 1%, 5% and 10% of samples are adopted as training set.

The accuracy increases in the wake of the increasing training samples, as we had expected. All 3D-based methods, including SSRN, FDSSC, DBMA, and proposed framework could obtain near-perfect performances whose OA can reach or exceed 99%, as long as sufficient samples (maybe 10% of the whole dataset) are rendered. At the same time, the performance gap between the disparate model is diminished following the increasing training samples inch by inch. Nevertheless, our method performs better than other methods, especially when samples are deficient, which means our method could offer acceptable classification results with limited labeled data when the expenditure of manual annotation is exorbitant.

4.4. Ablation Experiments

The utility of spatial attention mechanism and spectral attention mechanism is validated in the ablation experiments, in which three simplified DBDA framework, i.e., without spectral attention and spatial attention (denoted as without-attention), only with spatial attention (denoted as spatial-attention) and only with spectral attention (denoted as spectral-attention) are investigated.

The existence of spatial attention mechanism and spectral attention mechanism does promote the accuracy of four datasets, which can be concluded in Figure **Figure 12**. Furthermore, spatial attention mechanism performs more apparent effect upon most occasions.

4.5. Discussion

In this part, we attempt cautiously to illustrate the reason why our proposed framework works availably.

First, Dual Attention Network (DANet) [47], a flexible and adaptive self-attention mechanism module, is utilized to amplify the distinctiveness of spectral and spatial features. By a channel attention module and a position attention module, global dependencies in the spectral and spatial dimensions can be captured respectively. Even though DANet was designed for Scene Segmentation, the essence of Scene Segmentation and HSI classification can be viewed as classification at the pixel level. Based on the insight mentioned above, we have faith that more researches on the combination of these two fields would be implemented.

Second, Mish [48], a self-regularized non-monotonic activation function, is selected as the activation function of our framework. Compared with the classic ReLU, despite the computational complexity of Mish is higher than ReLU, the properties of Mish, including unbounded above, bounded below, smoothness, and non-monotonicity all dedicate ameliorations of convergence, which dose reduce time consumption prominently.

Preprints (www.preprints.org) | NOT PEER-REVIEWED | Posted: 5 December 2019 doi:10.20944/preprints201912.0059.v1

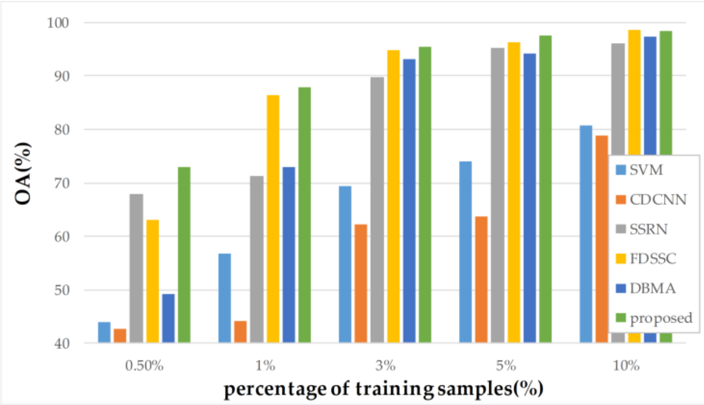

(a) Results on IP dataset using different percentages of training samples

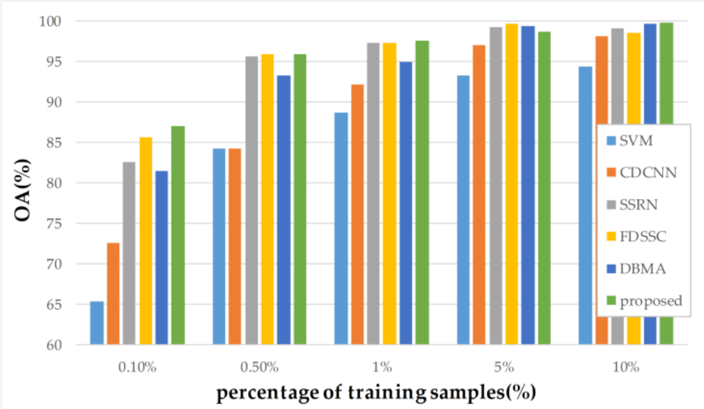

(b) Results on UP dataset using different percentages of training samples

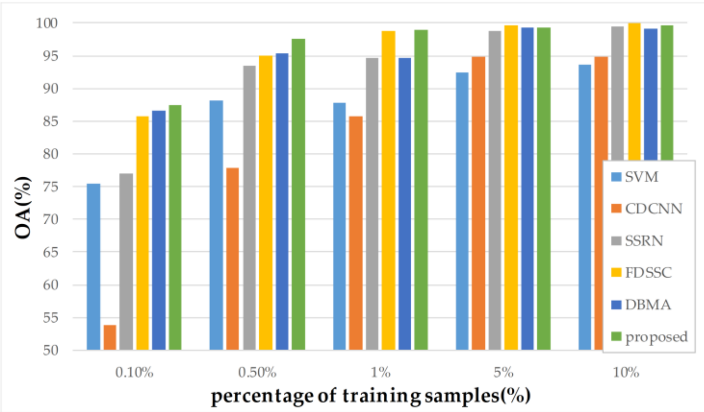

(c) Results on SV dataset using different percentages of training samples

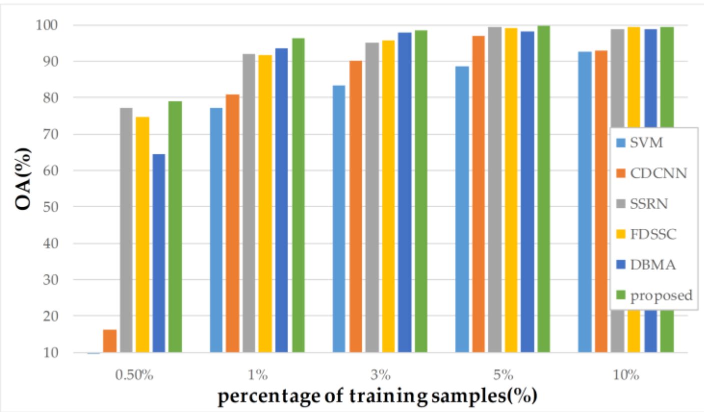

(d) Results on BS dataset using different percentages of training samples

Figure 11. The OA results of SVM, CDCNN, 3DCNN, SSRN, FDSSC, DBMA and proposed method with the different number of training samples on the (a) IP, (b) UP, (c) SV and (d) BS.

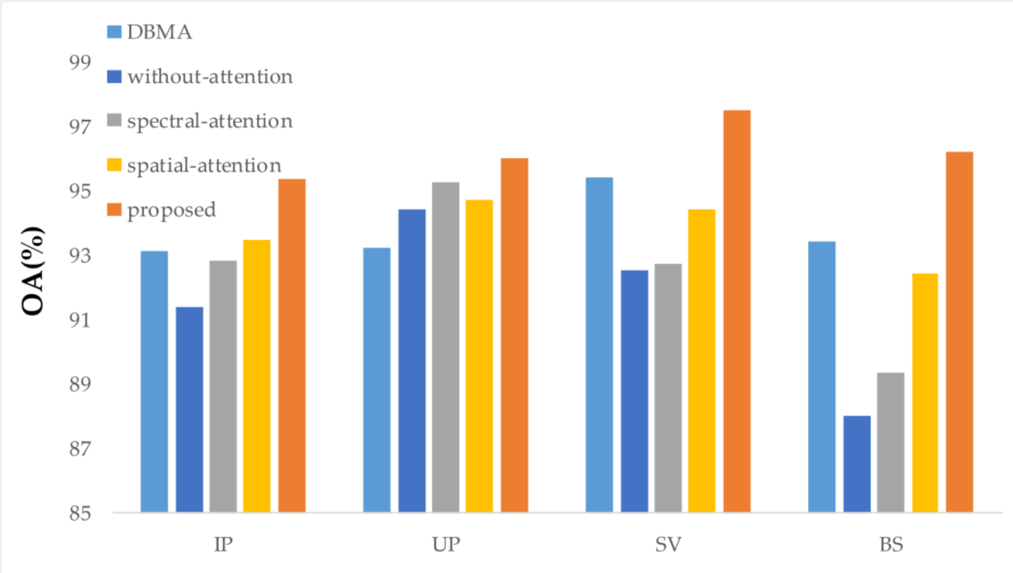

Figure 12. Ablation experiments about attention mechanisms on different datasets.

Third, dropout [50], a simple but effective skill to prevent overfitting, is affiliated to deal with the contradictions between numerous initialized parameters and limited training samples. As we analyzed earlier, DBMA [45] performs weaker than FDSSC [42] on two datasets when training samples are restrictive, which might be caused by the lack of dropout layers in DBMA.

5. Conclusions

In this paper, an end-to-end Double-Branch Dual-Attention mechanism network was proposed for HSI classification, which is equipped with two branches to capture spectral feature and spatial feature severally and densely connected 3D convolution layer to retard the disappearance of the gradient. Instead of cumbersome mechanism for reducing the dimensionality, we take the untreated 3D pixel data directly as input. Our work is based on the DBMA and DANet. DBMA is the state-of-the-art algorithm in HSI classification, and DANet is a flexible and adaptive self-attention mechanism in Scene Segmentation. Seemingly, a minor amelioration is obtained merely in this paper, but numerous empirical researches demonstrate that our proposed framework surpassed other state-of-the-art methods, especially when training samples are limited. Meanwhile, the consumption on time is also decreased contrasted with FDSSC and DBMA, as the attention blocks and the activation function Mish accelerate the convergence of the model.

The future direction of our work is generalizing our proposed framework to pragmatic hyperspectral data acquired recently, not just on the above-mentioned open-source datasets. Moreover, it is also an attractive challenge about how to compress the training time ulteriorly.

Acknowledgments: As this is the first time the first author, Rui Li, has written an article in English, in order to finish the draft as soon as possible, we take two papers that owned the same direction, *Double-Branch Multi-Attention Mechanism Network for Hyperspectral Image Classification* and *A Fast Dense Spectral–Spatial Convolution Network Framework for Hyperspectral Images Classification*, for reference. Therefore, the duplicate rate checking is a little high, maybe 30%, and we are revising our paper to the best of our ability. Thanks a million for the authors of the abovementioned papers, they are Wenping Ma, Qifan Yang, Yue Wu, Wei Zhao and Xiangrong Zhang who are the authors of the first paper, and Wenju Wang, Shuguang Dou, Zhongmin Jiang and Liujie Sun who are the authors of the second paper.

Funding: This research was funded by the National Natural Science Foundations of China (Nos. 41671452)

Conflicts of Interest: The authors declare no conflicts of interest. The founding sponsors had no role in the design of the study; in the collection, analyses, or interpretation of data; in the writing of the manuscript; nor in the decision to publish the results.

References

Preprints (www.preprints.org) | NOT PEER-REVIEWED | Posted: 5 December 2019 doi:10.20944/preprints201912.0059.v1

1. Zhong, Y.; Ma, A.; Ong, Y.; Zhu, Z; Zhang, L. Computational intelligence in optical remote sensing image processing. Applied Soft Computing, 2018, 64: 75-93.
2. Mahdianpari, M.; Salehi, B.; Rezaee, M.; Mohammadimanesh, F.; Zhang, Y. Very deep convolutional neural networks for complex land cover mapping using multispectral remote sensing imagery. Remote Sensing, 2018, 10(7): 1119.
3. Pipitone, C.; Maltese, A.; Dardanelli, G.; Brutto, M.; Loggia, G. Monitoring water surface and level of a reservoir using different remote sensing approaches and comparison with dam displacements evaluated via GNSS. Remote Sensing, 2018, 10(1): 71.
4. Zhao, C.; Wang Y.; Qi B.; Wang J. Global and local real-time anomaly detectors for hyperspectral remote sensing imagery. Remote Sensing, 2015, 7(4): 3966-3985.
5. Li, Z.; Huang, L.; He, J. A Multiscale Deep Middle-level Feature Fusion Network for Hyperspectral Classification. Remote Sensing, 2019, 11(6): 695.
6. Awad, M.; Jomaa, I.; Arab, F. Improved Capability in Stone Pine Forest Mapping and Management in Lebanon Using Hyperspectral CHRIS-Proba Data Relative to Landsat ETM+. Photogrammetric Engineering & Remote Sensing, 2014, 80(8): 725-731.
7. Ibrahim, A.; Franz, B.; Ahmad, Z.; Healy R.; Knobelspiesse, K.; Gao, B.; Proctor, C.; Zhai, P. Atmospheric correction for hyperspectral ocean color retrieval with application to the Hyperspectral Imager for the Coastal Ocean (HICO). Remote Sensing of Environment, 2018, 204: 60-75.
8. Marinelli, D.; Bovolo, F.; Bruzzone, L. A novel change detection method for multitemporal hyperspectral images based on binary hyperspectral change vectors. IEEE Transactions on Geoscience and Remote Sensing, 2019.
9. Melgani, F.; Bruzzone, L. Classification of hyperspectral remote sensing images with support vector machines. IEEE Transactions on geoscience and remote sensing, 2004, 42(8): 1778-1790.
10. Li, J.; Bioucas-Dias, J.; Plaza, A. Semisupervised hyperspectral image segmentation using multinomial logistic regression with active learning. IEEE Transactions on Geoscience and Remote Sensing, 2010, 48(11): 4085-4098.
11. Li, J.; Bioucas-Dias, J.; Plaza, A. Spectral–spatial hyperspectral image segmentation using subspace multinomial logistic regression and Markov random fields. IEEE Transactions on Geoscience and Remote Sensing, 2011, 50(3): 809-823.
12. Du, B.; Zhang, L. Random-selection-based anomaly detector for hyperspectral imagery. IEEE Transactions on Geoscience and Remote Sensing, 2010, 49(5): 1578-1589.
13. Du, B.; Zhang, L. Target detection based on a dynamic subspace. Pattern Recognition, 2014, 47(1): 344-358.
14. Li, J.; Marpu, P.; Plaza, A.; Bioucas-Dias, J.; Benediktsson, J. Generalized composite kernel framework for hyperspectral image classification. IEEE transactions on geoscience and remote sensing, 2013, 51(9): 4816-4829.
15. Li, W.; Du, Q. Gabor-filtering-based nearest regularized subspace for hyperspectral image classification. IEEE Journal of Selected Topics in Applied Earth Observations and Remote Sensing, 2014, 7(4): 1012-1022.
16. Fang, L.; Li, S.; Duan, W.; Ren, J.; Benediktsson, J. Classification of hyperspectral images by exploiting spectral–spatial information of superpixel via multiple kernels. IEEE transactions on geoscience and remote sensing, 2015, 53(12): 6663-6674.
17. Camps-Valls, G.; Gomez-Chova, L.; Muñoz-Marí, J.; Vila-Frances, J.; Calpe-Maravilla, J. Composite kernels for hyperspectral image classification. IEEE geoscience and remote sensing letters, 2006, 3(1): 93-97.
18. Fang, L.; He, N.; Li, S.; Ghamisi. P.; Benediktsson, J. Extinction profiles fusion for hyperspectral images classification. IEEE Transactions on Geoscience and Remote Sensing, 2017, 56(3): 1803-1815.
19. Li, P.; Chen, X.; Shen, S. Stereo r-cnn based 3d object detection for autonomous driving. Proceedings of the IEEE Conference on Computer Vision and Pattern Recognition. 2019: 7644-7652.
20. Zhang, W.; Feng, Y.; Meng, F.; You D.; Liu Q. Bridging the Gap between Training and Inference for Neural Machine Translation. arXiv preprint arXiv:1906.02448, 2019.
21. Durand, T.; Mehrasa, N.; Mori, G. Learning a Deep ConvNet for Multi-label Classification with Partial Labels. Proceedings of the IEEE Conference on Computer Vision and Pattern Recognition. 2019: 647-657.
22. Chen, Y.; Lin, Z.; Zhao, X.; Wang G.; Gu Y. Deep learning-based classification of hyperspectral data. IEEE Journal of Selected topics in applied earth observations and remote sensing, 2014, 7(6): 2094-2107.
23. Tao, C.; Pan, H.; Li, Y.; Zou Z. Unsupervised spectral–spatial feature learning with stacked sparse autoencoder for hyperspectral imagery classification. IEEE Geoscience and remote sensing letters, 2015, 12(12): 2438-2442.

Preprints (www.preprints.org) | NOT PEER-REVIEWED | Posted: 5 December 2019 doi:10.20944/preprints201912.0059.v1

24. Ma, X.; Wang, H.; Geng, J. Spectral–spatial classification of hyperspectral image based on deep auto-encoder. IEEE Journal of Selected Topics in Applied Earth Observations and Remote Sensing, 2016, 9(9): 4073-4085.
25. Zhang, X.; Liang, Y.; Li, C.; Hu, N.; Jiao, L; Zhou, H. Recursive autoencoders-based unsupervised feature learning for hyperspectral image classification. IEEE Geoscience and Remote Sensing Letters, 2017, 14(11): 1928-1932.
26. Chen, Y.; Zhao, X.; Jia, X. Spectral–spatial classification of hyperspectral data based on deep belief network. IEEE Journal of Selected Topics in Applied Earth Observations and Remote Sensing, 2015, 8(6): 2381-2392.
27. Makantasis, K.; Karantzalos, K.; Doulamis, A.; Doulamis, D. Deep supervised learning for hyperspectral data classification through convolutional neural networks. 2015 IEEE International Geoscience and Remote Sensing Symposium (IGARSS). IEEE, 2015: 4959-4962.
28. Zhao, W.; Du, S. Spectral–spatial feature extraction for hyperspectral image classification: A dimension reduction and deep learning approach[J]. IEEE Transactions on Geoscience and Remote Sensing, 2016, 54(8): 4544-4554.
29. Chen, Y.; Jiang, H.; Li, C.; Jia, X.; Ghamisi P. Deep feature extraction and classification of hyperspectral images based on convolutional neural networks. IEEE Transactions on Geoscience and Remote Sensing, 2016, 54(10): 6232-6251.
30. Li, Y.; Zhang, H.; Shen, Q. Spectral–spatial classification of hyperspectral imagery with 3D convolutional neural network. Remote Sensing, 2017, 9(1): 67.
31. Mou, L.; Ghamisi, P.; Zhu X. Deep recurrent neural networks for hyperspectral image classification. IEEE Transactions on Geoscience and Remote Sensing, 2017, 55(7): 3639-3655.
32. Tan, K.; Hu, J.; Li, J.; Du P. A novel semi-supervised hyperspectral image classification approach based on spatial neighborhood information and classifier combination. ISPRS journal of photogrammetry and remote sensing, 2015, 105: 19-29.
33. Zhang, M.; Gong, M; Mao, Y; Li, J.; Wu, Y. Unsupervised feature extraction in hyperspectral images based on wasserstein generative adversarial network. IEEE Transactions on Geoscience and Remote Sensing, 2018, 57(5): 2669-2688.
34. Haut, J.; Paoletti, M.; Plaza, J.; Li J.; Plaza, A. Active learning with convolutional neural networks for hyperspectral image classification using a new bayesian approach. IEEE Transactions on Geoscience and Remote Sensing, 2018, 56(11): 6440-6461.
35. Paoletti, M.; Haut, J.; Fernandez-Beltran, R.; Plaza, J.; Plaza, A.; Li, Jun.; Pla, F. Capsule networks for hyperspectral image classification. IEEE Transactions on Geoscience and Remote Sensing, 2018, 57(4): 2145-2160.
36. Yang, S.; Feng, Z.; Wang, M.; Zhang, K. Self-paced learning-based probability subspace projection for hyperspectral image classification. IEEE transactions on neural networks and learning systems, 2018, 30(2): 630-635.
37. Kemker, R.; Kanan, C. Self-taught feature learning for hyperspectral image classification. IEEE Transactions on Geoscience and Remote Sensing, 2017, 55(5): 2693-2705.
38. Chen, Z.; Jiang, J.; Zhou, C.; Fu S.; Cai, Z. SuperBF: Superpixel-Based Bilateral Filtering Algorithm and Its Application in Feature Extraction of Hyperspectral Images. IEEE Access, 2019, 7: 147796-147807.
39. He, K.; Zhang, X.; Ren, S.; Sun, J. Deep residual learning for image recognition. Proceedings of the IEEE conference on computer vision and pattern recognition. 2016: 770-778.
40. Huang, G.; Liu, Z.; Maaten, L.; Weinberger, K. Densely connected convolutional networks. Proceedings of the IEEE conference on computer vision and pattern recognition. 2017: 4700-4708.
41. Zhong, Z.; Li, J.; Luo, Z.; Chapman, M.; Weinberger Q. Spectral–spatial residual network for hyperspectral image classification: A 3-D deep learning framework. IEEE Transactions on Geoscience and Remote Sensing, 2017, 56(2): 847-858.
42. Wang, W.; Dou, S.; Jiang, Z.; Sun L. A Fast Dense Spectral–Spatial Convolution Network Framework for Hyperspectral Images Classification. Remote Sensing, 2018, 10(7): 1068.
43. Fang, B.; Li, Y.; Zhang, H.; Chan, J. Hyperspectral Images Classification Based on Dense Convolutional Networks with Spectral-Wise Attention Mechanism. Remote Sensing, 2019, 11(2): 159.
44. Woo, S.; Park, J.; Lee, J.; Kweon, I. Cbam: Convolutional block attention module. Proceedings of the European Conference on Computer Vision (ECCV). 2018: 3-19.
45. Ma, W.; Yang, Q.; Wu, Y.; Zhao, W.; Zhang X. Double-Branch Multi-Attention Mechanism Network for Hyperspectral Image Classification. Remote Sensing, 2019, 11(11): 1307.

Preprints (www.preprints.org) | NOT PEER-REVIEWED | Posted: 5 December 2019 doi:10.20944/preprints201912.0059.v1

46. Hou, R.; Chang, H.; Ma, B.; Shan, S.; Chen, X. Cross Attention Network for Few-shot Classification. arXiv preprint arXiv:1910.07677, 2019.
47. Fu, J.; Liu, J.; Tian, H.; Li, Y.; Bao, Y.; Fang, Z.; Lu H. Dual attention network for scene segmentation. Proceedings of the IEEE Conference on Computer Vision and Pattern Recognition. 2019: 3146-3154.
48. Misra, D. Mish: A Self Regularized Non-Monotonic Neural Activation Function. arXiv preprint arXiv:1908.08681, 2019.
49. Krizhevsky, A.; Sutskever, I.; Hinton, G. Imagenet classification with deep convolutional neural networks. Advances in neural information processing systems. 2012: 1097-1105.
50. Srivastava, N.; Hinton, G.; Krizhevsky, A.; Sutskever, I.; Salakhutdinov, R. Dropout: a simple way to prevent neural networks from overfitting. The journal of machine learning research, 2014, 15(1): 1929-1958.
51. Loshchilov, I.; Hutter, F. Sgdr: Stochastic gradient descent with warm restarts. arXiv preprint arXiv:1608.03983, 2016.
52. Rensink, R. The dynamic representation of scenes. Visual cognition, 2000, 7(1-3): 17-42.
53. Mnih, V.; Heess, N.; Graves A. Recurrent models of visual attention. Advances in neural information processing systems. 2014: 2204-2212.
54. Xu, K.; Ba, J.; Kiros, R.; Cho, K.; Courville, A.; Salakhutdinov, R.; Zemel, R.; Bengio, Y. Show, attend and tell: Neural image caption generation with visual attention. International conference on machine learning. 2015: 2048-2057.
55. Xu, T.; Zhang, P.; Huang, Q.; Zhang, H.; Gan, Z.; Huang, X.; He, X. Attngan: Fine-grained text to image generation with attentional generative adversarial networks. Proceedings of the IEEE Conference on Computer Vision and Pattern Recognition. 2018: 1316-1324.
56. Lee, H.; Kwon, H. Going deeper with contextual CNN for hyperspectral image classification. IEEE Transactions on Image Processing, 2017, 26(10): 4843-4855.
57. Melgani, F.; Bruzzone. L. Classification of hyperspectral remote sensing images with support vector machines. IEEE Transactions on geoscience and remote sensing, 2004, 42(8): 1778-1790.